#100

FERMILAB-CONF-74-148-E
SESSION A_3

Paper submitted to the XVII International Conference on High Energy Physics, Imperial College, London, 1-10 July 1974

Production of Hadrons with Large Transverse Momentum at 200, 300, and 400 GeV*

J. W. Cronin, H. J. Frisch, and M. J. Shochet
The Enrico Fermi Institute
University of Chicago, Chicago, Illinois 60637

and

J. P. Boymond, R. Mermod†, P. A. Piroué, and R. L. Sumner
Department of Physics, Joseph Henry Laboratories
Princeton University, Princeton, New Jersey 08540

ABSTRACT

We have measured, as a function of transverse momentum ($p_\perp$), the invariant cross section $Ed\sigma/d^3p$ for the production of $\pi^\pm$, $K^\pm$, p, $\bar{p}$, d, and $\bar{d}$ in p-nucleus collisions at incident proton energies of 200, 300, and 400 GeV. The measurements were made in the region of 90° in the c.m. system of the incident proton and a single nucleon at rest. At large values (> 0.40) of the scaling variable $x_\perp = 2p_\perp / \sqrt{s}$, where s is the square of the c.m. energy, the pion data are found to be well represented by an expression of the form $s^{-n}e^{-ax_\perp}$, with n = 5.5 ± 0.2 and a = 36.0 ± 0.4. At $x_\perp < 0.35$, where similar measurements have been made at the CERN ISR, our data are in excellent agreement with the ISR data. Results for other hadrons are presented.

In this paper we present further results on an experiment performed at the Fermi National Accelerator Laboratory on the production, in p-nucleus collisions, of long-lived hadrons ($\pi^{\pm}$, $K^{\pm}$, p, $\bar{p}$, d, and $\bar{d}$) with large transverse momenta ($p_{\perp}$). The measurements were made with a W target at incident proton energies of 200, 300, and 400 GeV, and in the region of 90° in the c.m. system of the incident proton and a single nucleon at rest. Some results, obtained at 200 and 300 GeV, have already been published[1]. Measurements were also made at 300 GeV with Be and Ti targets; they are reported in another paper[2] submitted to this conference.

The apparatus is shown schematically in Fig. 1. It is a single-arm magnetic spectrometer of 110 m length located at 77 mrad ($\sim$ 90° in the proton-nucleon c.m. system) relative to the incident proton beam. It is equipped with two 27-m-long Cerenkov counters of 2 channels each, 4 scintillation trigger counters (A), and 4 scintillation hodoscopes (H) used for reconstruction of particle tracks through the spectrometer back to the 2.16-cm-long, 0.64-cm-diam W target[3]. The momentum acceptance $\Delta p/p$ is $\pm$ 5% with a solid angle $\Delta\Omega$ = 17 μsr. A more detailed description of the experimental arrangement can be found in reference 1.

Runs were taken at laboratory momenta ranging from 10 to 120 GeV/c, corresponding to $p_{\perp}$ = 0.76 to 9.16 GeV/c. By use of the 4 Cerenkov channels pion, kaon, and proton yields could be measured concurrently. The Proton Laboratory where this experiment was performed is equipped with a beam splitting device which makes it possible to reduce the incident proton intensity by an arbitrary factor (to a minimum intensity as low as $\sim 10^{10}$ protons/burst). This feature permitted us to take data at very low momenta,

where the counting rates are very high, without switching to smaller trigger counters as we had to do at the beginning of the experiment when no beam splitting was possible[4]. Hence the accidental coincidences could be kept at a negligible level without any change in the apparatus.

Pion Production

The invariant cross sections per W nucleus, $Ed\sigma/d^3p$, for the production of $\pi^{\pm}$ in p-W collisions at incident proton energies of 200, 300, and 400 GeV are listed, as a function of $p_{\perp}$, in Table I. The data have been corrected for nuclear absorption in the apparatus and target (25%), for multiple Coulomb scattering (significant only below 1.5 GeV/c), and for pion decay (e.g., 16% at .76 GeV/c). The errors include the statistical errors (significant only at very high momenta) and the uncertainties introduced through the application of the above corrections and other systematic sources (momentum, solid angle, etc.). They do not include, however, the estimated 50% uncertainty in the calibration of the incident proton intensity[5].

For the purpose of comparison with p-p cross sections it is necessary to convert the cross sections per nucleus into equivalent p-nucleon cross sections. This conversion is model dependent. The simplest way, though not necessarily the best, is to divide the cross sections per nucleus by the atomic number A = 184 of W. Another method, which we used in our previous publication[1], is to divide the cross sections per nucleus by an effective number of nucleons defined as $A_{eff} = \sigma_{abs}/\sigma_p = 1635/40 = 40.9$, where σ_{abs} is the absorption cross section in W (1635 mb)

and σ_p is the p-p total cross section (40 mb). The best method, of course, is the one which yields cross sections independent of A. This point is discussed in reference 2.

In this paper, unless indicated otherwise, all cross sections shown in the figures are per effective nucleon, and thus have been obtained by dividing the cross sections per nucleus of Table I by 40.9.

Figures 2 and 3 show the π^+ and π^- invariant cross sections, respectively, plotted against $p_\perp$ at 200, 300, and 400 GeV. For all energies and at large $p_\perp$ the cross sections fall exponentially; they do not show a manifest power law dependence. The energy dependence, very small at low $p_\perp$, grows stronger as $p_\perp$ increases. This is in agreement with the work done at ISR by the Saclay-Strasbourg group[6], the CERN-Columbia-Rockefeller group[7], and the British-Scandinavian Collaboration[8], and at NAL by Carey et al.[9]

Most of the theoretical models[10] which have been proposed predict for the single-pion inclusive cross section at $\sim 90°$ c.m. a behavior, at high $p_\perp$, of the form $g(s)f(x_\perp)$[11], where $g(s)$ is some function (generally a power law) of s, the square of the c.m. energy of the collision, and $f(x_\perp)$ is a function of the scaling variable $x_\perp = 2p / \sqrt{s}$. If our pion data can indeed be expressed in such a form, then the logarithm of the cross section plotted against $x_\perp$ at all 3 energies should yield parallel curves, irrespective of the absolute calibration. Figures 4 and 5 show that this is definitely so at $x_\perp > 0.40$; moreover $f(x_\perp)$ has in this region the simple exponential form $e^{-ax_\perp}$. At $x_\perp < 0.35$, however, the curves are slowly converging as $x_\perp$ decreases. Figure 5 shows clearly that the

scaling region starts at fixed $x_\perp$ ($\sim$ 0.40) rather than fixed $p_\perp$.

In the scaling region ($x_\perp > 0.40$) a very good fit is obtained, as seen in Fig. 6, when the data at all 3 energies are fitted to the expression

$$Ed\sigma/d^3p \propto s^{-n} e^{-ax_\perp}.$$

We obtain for π^+ : $n = 5.7 \pm 0.2$, $a = 36.3 \pm 0.4$;

for π^- : $n = 5.4 \pm 0.2$, $a = 36.0 \pm 0.4$

(Systematic uncertainties completely dominate the errors.)

Comparison with ISR data. As we show in another paper submitted to this conference[2], the invariant cross section for hadron production in effective p-nucleon collisions still depends on the atomic number A. Tungsten, for example, is much more efficient than Be in producing large transverse momentum hadrons. In the scaling region, however, only the absolute cross section (not the shape) is affected. In any case Be should provide a more reliable comparison with the ISR data than W. In Fig. 7 we compare the π^0 data of the CERN-Columbia-Rockefeller (CCR) group[7] with the average of the π^+ and π^- cross sections which we obtained with a Be target[12]. At $\sqrt{s}$ = 23.8 and 23.5 GeV, where the data can be directly compared, the agreement is very good indeed. (At low $p_\perp$, where the s dependence is very small, our data agree also very well with those of the Saclay-Strasbourg[6] and British-Scandinavian[8] collaborations.)

In the scaling region ($x_\perp > 0.40$), where our data are well represented by the expression

$$Ed\sigma/d^3p \propto s^{-5.5} e^{-36x_\perp},$$

there are no data from the ISR, and hence no comparison is possible. It is interesting to note, however, that in the interval $0.1 < x_\perp < 0.35$, where the CCR data show an energy dependence of $s^{-4.1}$, our cross sections have an energy dependence ranging from $s^{-2.9}$ at $x_\perp = 0.1$ to $s^{-5.4}$ at $x_\perp = 0.35$, with an average of $\sim s^{-4.25}$, in good agreement with the CCR result. This point is illustrated in Fig. 8 where we show as a function of $x_\perp$, the value n obtained from the fit of the Be cross sections to $s^{-n} f(x_\perp)$. This result suggests that if the ISR measurements were extended beyond $x_\perp = 0.40$, they might exhibit a scaling behavior similar to our data, in particular an energy dependence $\sim s^{-5.5}$.

Kaon Production

The $K^\pm$ yields relative to pions of the same charge are given in Table II. Figure 9 shows those ratios as functions of $p_\perp$. We see that K^+/π^+ is essentially independent of s, rising from ~ 0.2 at $p_\perp = 0.76$ GeV/c to $\sim$ 0.55 at 4 GeV/c and beyond. The K^-/π^- ratio, also independent of s within the errors at very low $p_\perp$ (< 1 GeV/c), does have, however, a definite energy dependence at $p_\perp >$ 2 GeV/c. In fact, in this region, it is rather well represented by an expression of the form $\sqrt{s}\, F(p_\perp)$, where $F(p_\perp)$ is a slowly varying function with a broad maximum at $p \approx 2.5$ GeV/c and dropping by a factor of ~ 2 at $p \approx 6$ GeV/c. It may be appropriate here to note that the $\bar{p}/\pi^-$ ratio has a similar behavior, in particular a $\sqrt{s}$ dependence ($F(p_\perp)$, however, drops off faster).

If the $K^\pm/\pi^\pm$ ratios are plotted against the scaling variable $x_\perp = 2p_\perp/\sqrt{s}$, as in Fig. 10, one sees from the K^+/π^+ behavior that the

K^+ cross section scales in the same way as the pions. At $x_\perp > 0.40$ a fit of the K^+ cross sections to $s^{-n}e^{-ax_\perp}$ yields

$$n = 5.3 \pm 0.4 \text{ and } a = 35.0 \pm 1.5,$$

in agreement, within the errors, with the pion values.

The K^-/π^- ratio, on the contrary, does not appear to scale although this cannot be completely ruled out because, at $x_\perp > 0.45$, the errors could conceivably accommodate parallel curves.

Finally, it should be noted that our kaon data are in agreement with the results of the British-Scandinavian Collaboration[13]. (For example, at $p_\perp = 0.5$ GeV/c and $\sqrt{s} = 30.6$ GeV they obtained $K^+/\pi^+ = 0.17$ and $K^-/\pi^- = 0.13$.)

Proton and Antiproton Production

In Table III we give the proton and antiproton yields relative to pions of the same charge. A plot of these ratios as a function of $p_\perp$ is shown in Fig. 11. As $p_\perp$ decreases from $\sim$ 1.5 GeV/c both ratios decrease and tend to become s independent. This feature, also observed with kaons, indicates that the invariant cross sections of particles heavier than pions do not rise with decreasing $p_\perp$ as fast as pions in this region. In fact, the $K^\pm$, p, and $\bar{p}$ cross sections plotted against $p_\perp$ fall off almost exponentially all the way from $\sim$ 1 to 7 GeV/c, the protons showing the smallest s dependence.

As already mentioned above the $\bar{p}/\pi^-$ ratio shows, at $p_\perp = 1.5$ GeV/c, the same $\sqrt{s}$ dependence at fixed $p_\perp$ as the K^-/π^- ratio, but it falls off

faster with increasing $p_\perp$, dropping by a factor of $\sim$ 10 from $p_\perp$ = 1.5 to 6 GeV/c.

When plotted against $x_\perp$, as in Fig. 12, neither the p/π^+ nor the $\bar{p}/\pi^-$ ratio seems to scale as the pions and K^+ do. However, the errors are again sufficiently large, especially in the case of $\bar{p}/\pi^-$, to accommodate nearly parallel curves at $x_\perp > 0.45$.

As with kaons our p and $\bar{p}$ results agree with those of the British-Scandinavian Collaboration[13] who, at $p_\perp$ = 0.5 GeV/c and $\sqrt{s}$ = 30.6 GeV measured $p/\pi^+ = 0.15$ and $\bar{p}/\pi^- = 0.07$. The comparison between the proton data should not be taken too literally though because there is evidence, as seen in reference 2, that nuclear matter has a significant influence on the p/π^+ ratio.

Deuteron and Antideuteron Production

In Table IV we present the d/π^+, $\bar{d}/\pi^-$, d/p, and $\bar{d}/\bar{p}$ ratios obtained at 300 GeV. The d/π^+ and $\bar{d}/\pi^-$ ratios are also displayed in Fig. 11.

A direct comparison of our $\bar{d}$ cross sections with data obtained at the ISR[14] and NAL[15] is difficult because they were measured under quite different conditions. At 300 GeV Appel et al.[15] obtained with a W target and in the forward direction ($p_\perp$ = 0) at 30 GeV/c lab. momentum, a ratio $\bar{d}/\pi^- \approx 10^{-5}$. At the ISR the British-Scandinavian Collaboration[14] observed $\bar{d}/\pi^- = 5 \times 10^{-5}$ at $p_\perp$ = 0.7 GeV/c and $\sqrt{s}$ = 53 GeV. We observe $\bar{d}/\pi^- = 1.4 \times 10^{-4}$ at $p_\perp$ = 2.3 GeV/c. This large relative yield seems to confirm what had already been apparent with $\bar{p}$ production, namely, that heavy particles are more copiously produced relative to pions at high $p_\perp$.

However, heavy antiparticle production falls off faster with increasing $p_\perp$ than their counterpart. This feature is illustrated in Fig. 13.

Many models[16-19] have been proposed and tested to explain deuteron (and antideuteron) formation at lower energies. A mechanism which seems to account roughly for the observed rates involves the pairing of a neutron (antineutron) and a proton (antiproton) of approximately equal momenta. The characteristics of all these models is that they provide a connection between the number of deuterons (antideuterons) emerging at a given angle and momentum, and the corresponding number of protons (antiprotons) at that angle but at <u>half</u> that momentum. A direct consequence of such models, already put to a test when antideuterons were first observed[19], is the following relation:

$$\frac{d}{\bar{d}}(p') \cong \left[\frac{p}{\bar{p}}(p'/2)\right]^2 ,$$

where p' is the emerging deuteron (antideuteron) momentum. It is clear from Fig. 13 that such a relation is reasonably well satisfied, within the errors, by our 300-GeV data.

We wish to express our gratitude to the staff of the Fermi National Accelerator Laboratory, and especially of the Proton Section, for their invaluable cooperation throughout the course of this experiment. One of us (R.M.) would like to thank the Laboratory for its hospitality and support.

REFERENCES

*Work supported by the National Science Foundation and the U. S. Atomic Energy Commission.

†On leave at NAL from the University of Geneva.

1. J. W. Cronin et al., Phys. Rev. Letters 31, 1426 (1973).
2. J. W. Cronin et al., "Atomic Number Dependence of Hadron Production at Large Transverse Momentum in 300-GeV Proton-Nucleus Collisions", paper submitted to this Conference, Session A_3.
3. Some data have been taken with a 5.08-cm-long, 0.32-cm-diam target.
4. As a result the very low momenta have been slightly revised from those of Ref.1 .
5. A more precise determination of the incoming proton beam intensity changed the cross sections published in Ref. 1 by an overall factor of $\sim$ 1.6.
6. M. Banner et al., Phys. Letters 41B, 547 (1972); 44B, 537 (1973).
7. F. W. Büsser et al., Phys. Letters 46B, 471 (1973).
8. B. Alper et al., Phys. Letters 44B, 521 (1973); 44B, 527 (1973).
9. D. C. Carey et al., Phys. Rev. Letters 32, 24 (1974).
10. See, for example, S. M. Berman, J. D. Bjorken, and J. B. Kogut, Phys. Rev. D4, 3388 (1971); R. Blankenbecler, S. J. Brodsky, and J. F. Gunion, Phys. Letters 42B, 461 (1972); P. V. Landshoff and J. C. Polkinghorne, Phys. Letters 45B, 361 (1973); S. D. Ellis and M. B. Kislinger, NAL Report No. PUB-73/40/THY (1973), to be published in Phys. Rev.; S. D. Ellis, Phys. Letters 49B, 189 (1974); P. V. Landshoff and J. C. Polkinghorne, Phys. Rev. D8, 297 (1973).

11. In a recent preprint, J. F. Gunion, S. J. Brodsky, and R. Blankenbecler, University of Pittsburg PITT-124, proposed a function of the form $s^{-4}(F(x_\perp) + s^{-2}G(x_\perp))$.

12. The Be data were obtained at 300 GeV. The 200- and 400-GeV curves were calculated by assuming at each energy the same ratio between W and Be as at 300 GeV.

13. B. Alper et al., Phys. Letters 47B, 275 (1973); 47B, 75 (1973).

14. B. Alper et al., Phys. Letters 46B, 265 (1973).

15. J. A. Appel et al., Phys. Rev. Letters 32, 428 (1974).

16. S. T. Butler and C. A. Pearson, Phys. Rev. Letters 7, 69 (1961); 1, 77 (1962); Phys. Rev. 129, 836 (1963).

17. A. Schwarzschild and Č. Zupancič, Phys. Rev. 129, 854 (1963).

18. P. A. Piroué and A. J. S. Smith, Phys. Rev. 148, 1315 (1966).

19. D. E. Dorfan et al., Phys. Rev. Letters 14, 1003 (1965).

FIGURE CAPTIONS

Fig. 1. Experimental arrangement

Fig. 2. Invariant cross section per effective nucleon (see text) for π^+ mesons produced at $\sim 90°$ c.m. in p-W collisions.

Fig. 3. Invariant cross section per effective nucleon for π^- mesons produced at $\sim 90°$ c.m. in p-W collisions.

Fig. 4. π^- production cross section versus $x_\perp$.

Fig. 5. π^- production cross section versus $x_\perp$ in the scaling region.

Fig. 6. Plot of the function $s^{5.4}Ed\sigma(\pi^-)/d^3p$ versus $x_\perp$.

Fig. 7. The average of the π^+ and π^- invariant cross sections per effective nucleon in p-Be collisions, and the π^0 cross section in p-p collisions.

Fig. 8. The exponent n obtained from the fit of the function $s^{-n}f(x_\perp)$ to the average $\pi^\pm$ cross sections shown in Fig. 7.

Fig. 9. Kaon abundance relative to pions versus $p_\perp$.

Fig.10. Kaon abundance relative to pions versus $x_\perp = 2p/\sqrt{s}$.

Fig.11. Proton, antiproton, deuteron, and antideuteron abundances relative to pions of the same charge versus $p_\perp$.

Fig.12. Proton and antiproton abundances relative to pions versus $x_\perp = 2p_\perp/\sqrt{s}$.

Fig.13. Particle-antiparticle ratios versus $p_\perp$.

TABLE CAPTIONS

Table I. Invariant cross section per nucleus for $\pi^{\pm}$ mesons produced at $\sim 90°$ c.m. in p-W collisions. At each $p_{\perp}$ value the top line refers to π^+ and the bottom line to π^-. Errors do not include the uncertainty in the absolute calibration. Cross sections per effective nucleon (see text) are obtained by dividing the listed cross sections by 40.9.

[a]90% confidence limit

Table II. K^+/π^+ (top line) and K^-/π^- (bottom line) cross section ratios.

Table III. p/π^+ (top line) and $\bar{p}/\pi^-$ (bottom line) cross section ratios.

Table IV. d/π^+, d/p (top line) and $\bar{d}/\pi^-$, $\bar{d}/\bar{p}$ (bottom line) cross section ratios.

$p_\perp$ (GeV/c)	$Ed\sigma(\pi^\pm)/d^3p$ ($cm^2 GeV^{-2}$) 200 GeV	300 GeV	400 GeV
0.76	1.22 ± 0.12 1.13 ± 0.11 $\times 10^{-25}$	1.36 ± 0.14 1.39 ± 0.14 $\times 10^{-25}$	1.61 ± 0.16 1.50 ± 0.15 $\times 10^{-25}$
1.14	2.34 ± 0.12 1.74 ± 0.09 $\times 10^{-26}$	2.44 ± 0.12 2.24 ± 0.11 $\times 10^{-26}$	2.48 ± 0.12 2.16 ± 0.11 $\times 10^{-26}$
1.53	3.81 ± 0.19 2.83 ± 0.14 $\times 10^{-27}$	3.96 ± 0.20 3.77 ± 0.19 $\times 10^{-27}$	4.21 ± 0.21 3.87 ± 0.19 $\times 10^{-27}$
2.29	1.73 ± 0.09 1.25 ± 0.06 $\times 10^{-28}$	2.00 ± 0.10 1.83 ± 0.09 $\times 10^{-28}$	2.21 ± 0.11 1.99 ± 0.10 $\times 10^{-28}$
3.05	8.35 ± 0.42 6.55 ± 0.33 $\times 10^{-30}$	1.18 ± 0.06 1.06 ± 0.05 $\times 10^{-29}$	1.50 ± 0.07 1.33 ± 0.07 $\times 10^{-29}$
3.82	4.54 ± 0.23 3.35 ± 0.17 $\times 10^{-31}$	8.63 ± 0.43 7.73 ± 0.39 $\times 10^{-31}$	1.13 ± 0.06 0.98 ± 0.05 $\times 10^{-30}$
4.58	2.58 ± 0.13 1.91 ± 0.10 $\times 10^{-32}$	6.29 ± 0.31 5.97 ± 0.30 $\times 10^{-32}$	1.05 ± 0.05 0.86 ± 0.04 $\times 10^{-31}$
5.34	1.59 ± 0.08 1.11 ± 0.06 $\times 10^{-33}$	6.46 ± 0.32 5.27 ± 0.26 $\times 10^{-33}$	1.04 ± 0.05 0.86 ± 0.04 $\times 10^{-32}$
6.10	8.7 ± 1.2 7.07 ± 0.82 $\times 10^{-35}$	6.43 ± 0.32 5.12 ± 0.26 $\times 10^{-34}$	1.39 ± 0.07 1.16 ± 0.06 $\times 10^{-33}$
6.87	4.5 ± 1.1 3.5 ± 1.0 $\times 10^{-36}$	5.12 ± 0.69 $\times 10^{-35}$	1.78 ± 0.11 1.58 ± 0.09 $\times 10^{-34}$
7.25	1.1 ± 0.6 $\times 10^{-36}$		
7.63		4.6 ± 1.3 5.5 ± 1.3 $\times 10^{-36}$	2.39 ± 0.40 2.31 ± 0.34 $\times 10^{-35}$
8.39		4.4 ± 2.6 $\times 10^{-37}$	2.5 ± 0.7 3.2 ± 1.1 $\times 10^{-36}$
9.16		< 8.9 $\times 10^{-38}$ [a]	

Table I

$p_\perp$ (GeV/c)	PARTICLE RATIO $K^\pm/\pi^\pm$ 200 GeV	300 GeV	400 GeV
0.76	0.24 ± 0.04 0.15 ± 0.03	0.21 ± 0.02 0.14 ± 0.02	0.23 ± 0.03 0.15 ± 0.04
1.14	0.32 ± 0.03 0.20 ± 0.02	0.31 ± 0.02 0.20 ± 0.02	0.31 ± 0.03 0.22 ± 0.02
1.53	0.39 ± 0.03 0.200 ± 0.014	0.360 ± 0.016 0.202 ± 0.008	0.395 ± 0.028 0.225 ± 0.016
2.29	0.445 ± 0.024 0.207 ± 0.010	0.433 ± 0.018 0.242 ± 0.010	0.439 ± 0.028 0.282 ± 0.019
3.05	0.485 ± 0.015 0.201 ± 0.006	0.506 ± 0.019 0.248 ± 0.010	0.500 ± 0.026 0.274 ± 0.011
3.82	0.522 ± 0.024 0.191 ± 0.007	0.543 ± 0.020 0.230 ± 0.009	0.543 ± 0.029 0.248 ± 0.008
4.58	0.536 ± 0.033 0.170 ± 0.014	0.535 ± 0.022 0.198 ± 0.008	0.490 ± 0.030 0.222 ± 0.009
5.34	0.64 ± 0.07 0.15 ± 0.03	0.531 ± 0.035 0.167 ± 0.008	0.712 ± 0.044 0.188 ± 0.010
6.10	0.55 ± 0.19 0.08 ± 0.07	0.53 ± 0.05 0.115 ± 0.011	0.66 ± 0.06 0.112 ± 0.022
6.87		0.10 ± 0.03	0.71 ± 0.15 0.060 ± 0.023
7.63		0.05 ± 0.05	

Table II

$p_\perp$ (GeV/c)	PARTICLE RATIO p/π 200 GeV	300 GeV	400 GeV
0.76	0.43 ± 0.02 0.105 ± 0.030	0.34 ± 0.02 0.08 ± 0.01	0.35 ± 0.02 0.07 ± 0.01
1.14	0.632 ± 0.006 0.107 ± 0.005	0.531 ± 0.020 0.105 ± 0.005	0.530 ± 0.010 0.127 ± 0.002
1.53	0.834 ± 0.009 0.109 ± 0.002	0.669 ± 0.020 0.126 ± 0.004	0.685 ± 0.010 0.146 ± 0.003
2.29	1.033 ± 0.012 0.095 ± 0.003	0.872 ± 0.020 0.115 ± 0.002	0.811 ± 0.015 0.139 ± 0.004
3.05	1.093 ± 0.011 0.076 ± 0.001	0.865 ± 0.008 0.089 ± 0.002	0.788 ± 0.016 0.102 ± 0.003
3.82	1.07 ± 0.02 0.044 ± 0.003	0.827 ± 0.020 0.061 ± 0.002	0.689 ± 0.018 0.076 ± 0.003
4.58	1.11 ± 0.03 0.033 ± 0.003	0.736 ± 0.020 0.041 ± 0.002	0.616 ± 0.018 0.047 ± 0.003
5.34	1.09 ± 0.07 0.029 ± 0.014	0.60 ± 0.02 0.023 ± 0.002	0.553 ± 0.024 0.032 ± 0.004
6.10	0.98 ± 0.17 < 0.01	0.56 ± 0.04 0.013 ± 0.003	0.38 ± 0.03 0.011 ± 0.005
6.87		0.01 ± 0.01	0.36 ± 0.08 0.006 ± 0.006

Table III

$p_\perp$ (GeV/c)	300 GeV d/π	d/p
2.29	$\begin{matrix} 47 \pm 5 \\ 1.42 \pm 0.14 \end{matrix} \times 10^{-4}$	$\begin{matrix} 5.4 \pm 0.6 \\ 1.23 \pm 0.12 \end{matrix} \times 10^{-3}$
3.05	$\begin{matrix} 66 \pm 6 \\ 1.0 \pm 0.1 \end{matrix} \times 10^{-4}$	$\begin{matrix} 7.6 \pm 0.8 \\ 1.12 \pm 0.11 \end{matrix} \times 10^{-3}$
3.82	$\begin{matrix} 52 \pm 5 \\ 0.91 \pm 0.15 \end{matrix} \times 10^{-4}$	$\begin{matrix} 6.3 \pm 0.6 \\ 1.49 \pm 0.25 \end{matrix} \times 10^{-3}$
4.58	$\begin{matrix} 45 \pm 5 \\ 0.22 \pm 0.13 \end{matrix} \times 10^{-4}$	$\begin{matrix} 6.1 \pm 0.6 \\ 0.54 \pm 0.32 \end{matrix} \times 10^{-3}$
5.34	$26 \pm 11 \times 10^{-4}$	$4.3 \pm 1.8 \times 10^{-3}$

Table IV

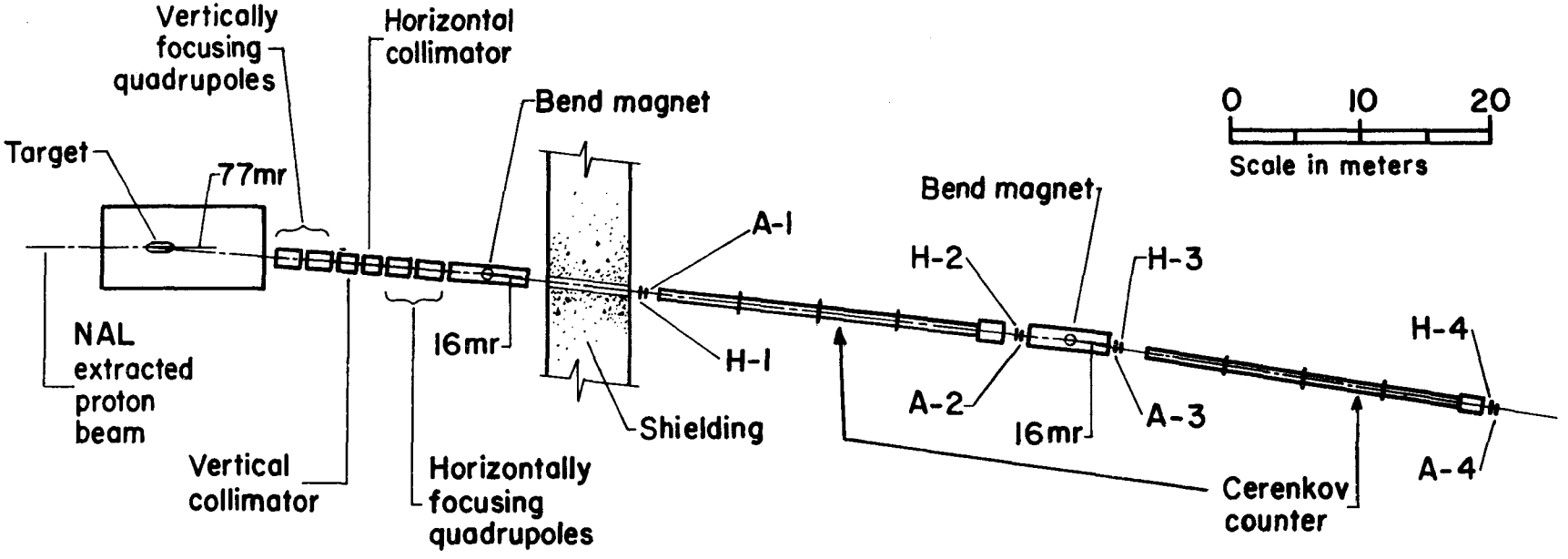
Vertically
focusing
quadrupoles
Horizontal
collimator
Bend magnet
0
10
20
Scale in meters
Target
77mr
Bend magnet
A-1
H-2
H-3
H-4
NAL
extracted
proton
beam
16mr
H-1
A-2
A-3
16mr
A-4
Shielding
Vertical
collimator
Horizontally
focusing
quadrupoles
Cerenkov
counter

FIGURE 1

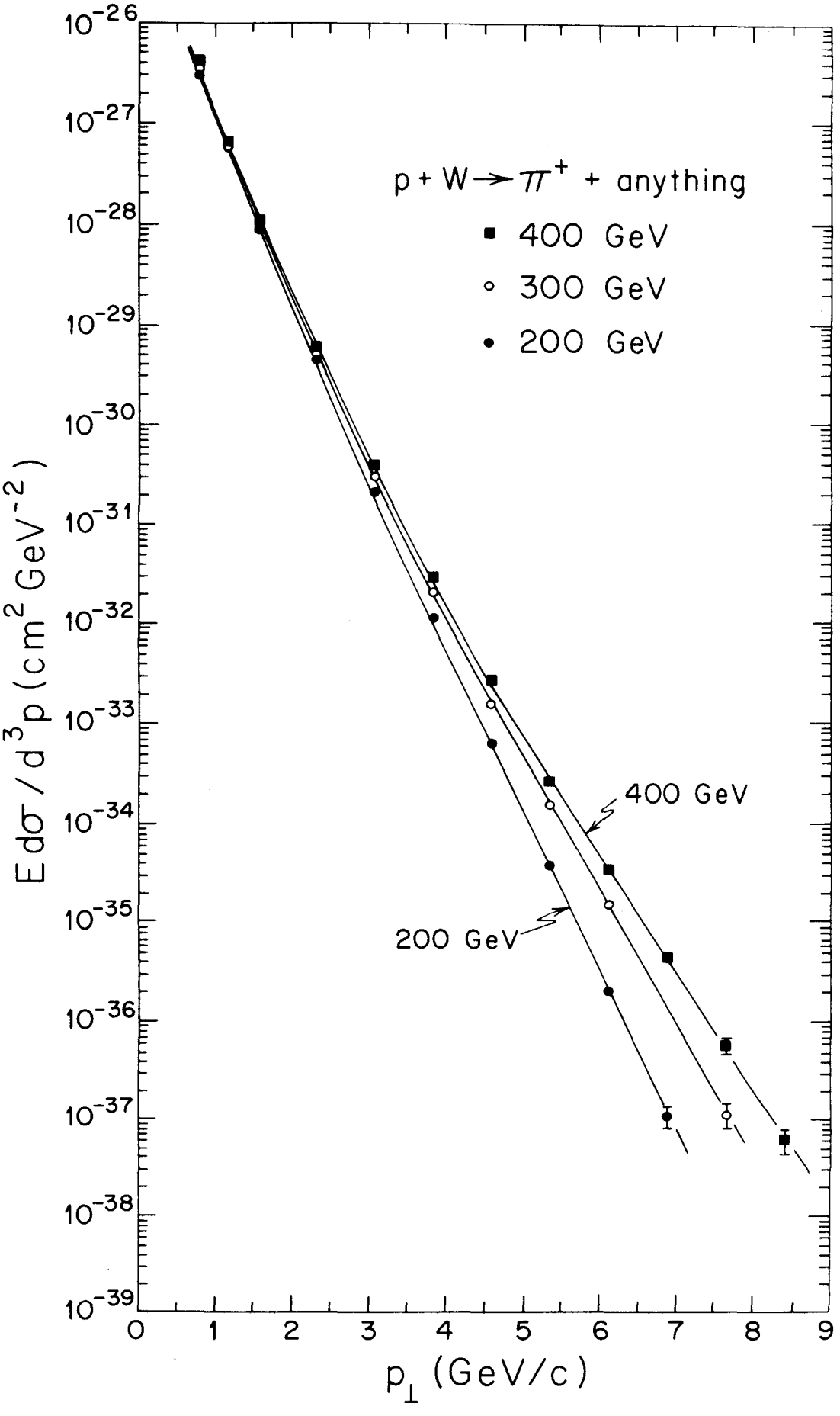
10^{-26}
10^{-27}
10^{-28}
10^{-29}
10^{-30}
10^{-31}
10^{-32}
10^{-33}
10^{-34}
10^{-35}
10^{-36}
10^{-37}
10^{-38}
10^{-39}
$E d\sigma / d^3p$ (cm^2 GeV^{-2})
0
1
2
3
4
5
6
7
8
9
$p_\perp$ (GeV/c)
$p + W \rightarrow \pi^+ +$ anything
400 GeV
300 GeV
200 GeV
400 GeV
200 GeV

FIGURE 2

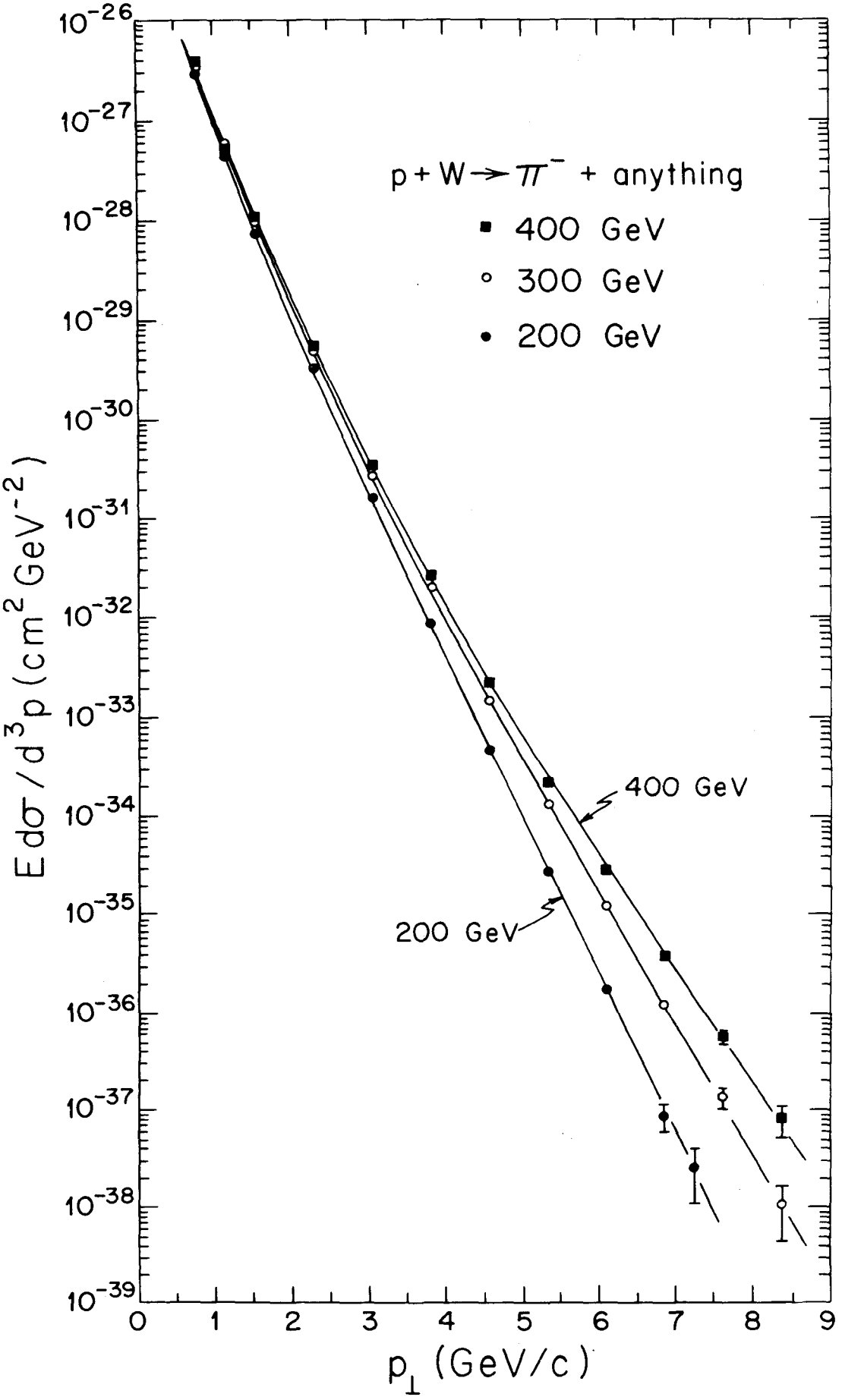
$p + W \rightarrow \pi^- +$ anything
400 GeV
300 GeV
200 GeV
400 GeV
200 GeV
$E d\sigma / d^3p$ (cm^2 GeV^{-2})
$p_\perp$ (GeV/c)
10^{-26}
10^{-27}
10^{-28}
10^{-29}
10^{-30}
10^{-31}
10^{-32}
10^{-33}
10^{-34}
10^{-35}
10^{-36}
10^{-37}
10^{-38}
10^{-39}
0
1
2
3
4
5
6
7
8
9

FIGURE 3

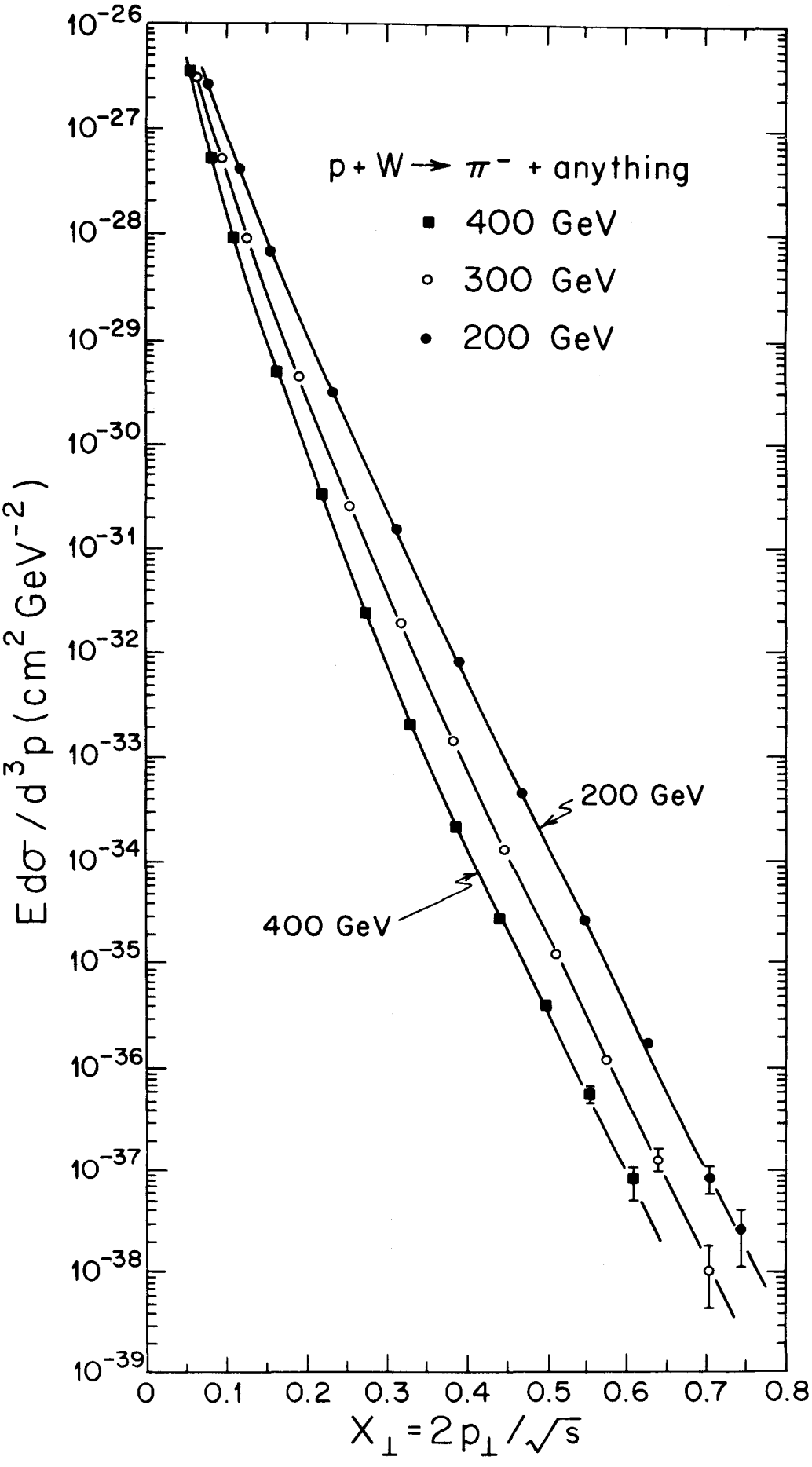
10^{-26}
10^{-27}
10^{-28}
10^{-29}
10^{-30}
10^{-31}
10^{-32}
10^{-33}
10^{-34}
10^{-35}
10^{-36}
10^{-37}
10^{-38}
10^{-39}
$E d\sigma / d^3p\ (cm^2\ GeV^{-2})$
$p + W \rightarrow \pi^- +$ anything
400 GeV
300 GeV
200 GeV
200 GeV
400 GeV
0
0.1
0.2
0.3
0.4
0.5
0.6
0.7
0.8
$X_\perp = 2p_\perp / \sqrt{s}$

FIGURE 4

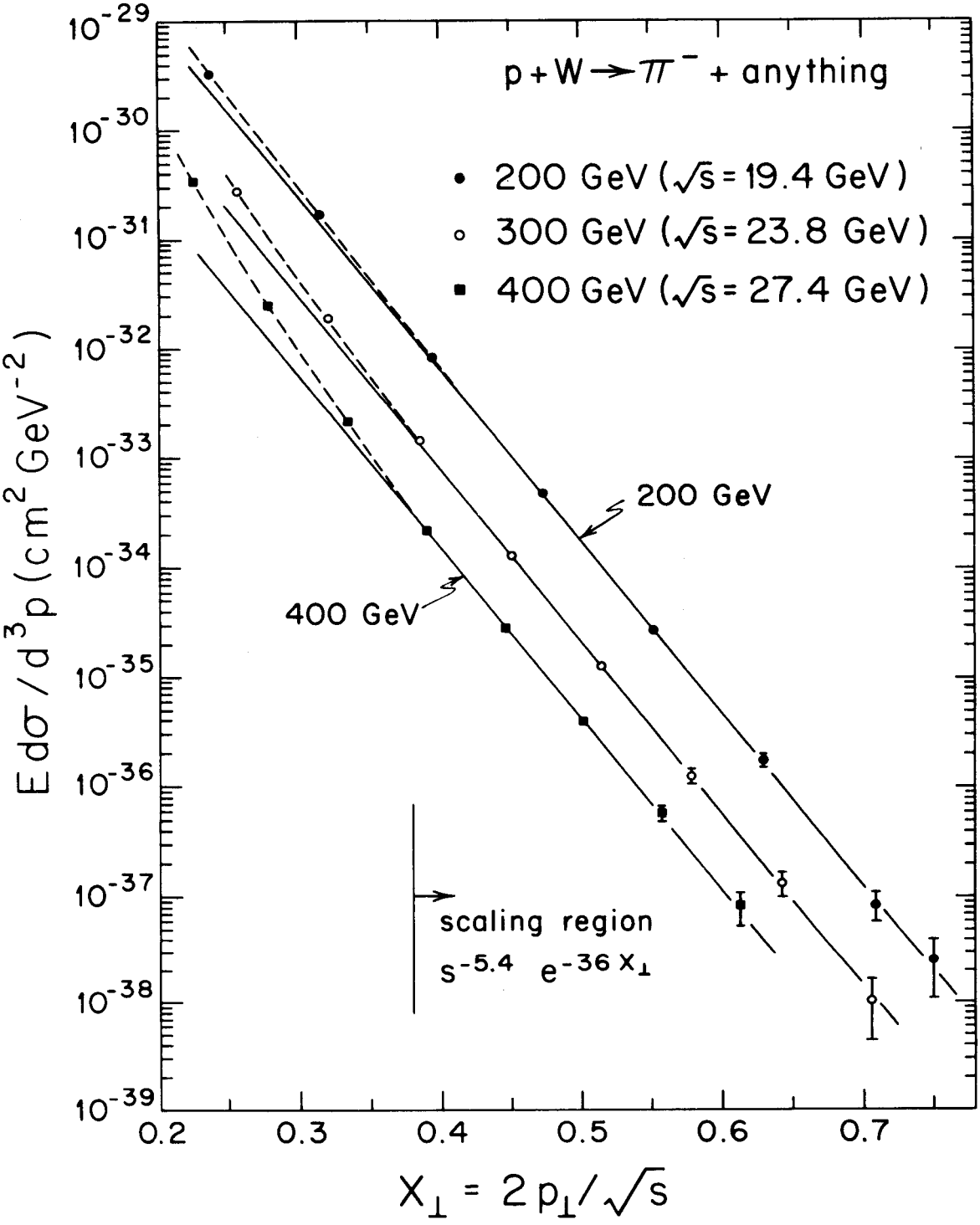
p + W → π⁻ + anything
200 GeV (√s = 19.4 GeV)
300 GeV (√s = 23.8 GeV)
400 GeV (√s = 27.4 GeV)
200 GeV
400 GeV
scaling region
s^-5.4 e^-36 x⊥
E dσ/d³p (cm² GeV⁻²)
X⊥ = 2p⊥/√s
10^-29
10^-30
10^-31
10^-32
10^-33
10^-34
10^-35
10^-36
10^-37
10^-38
10^-39
0.2
0.3
0.4
0.5
0.6
0.7

FIGURE 5

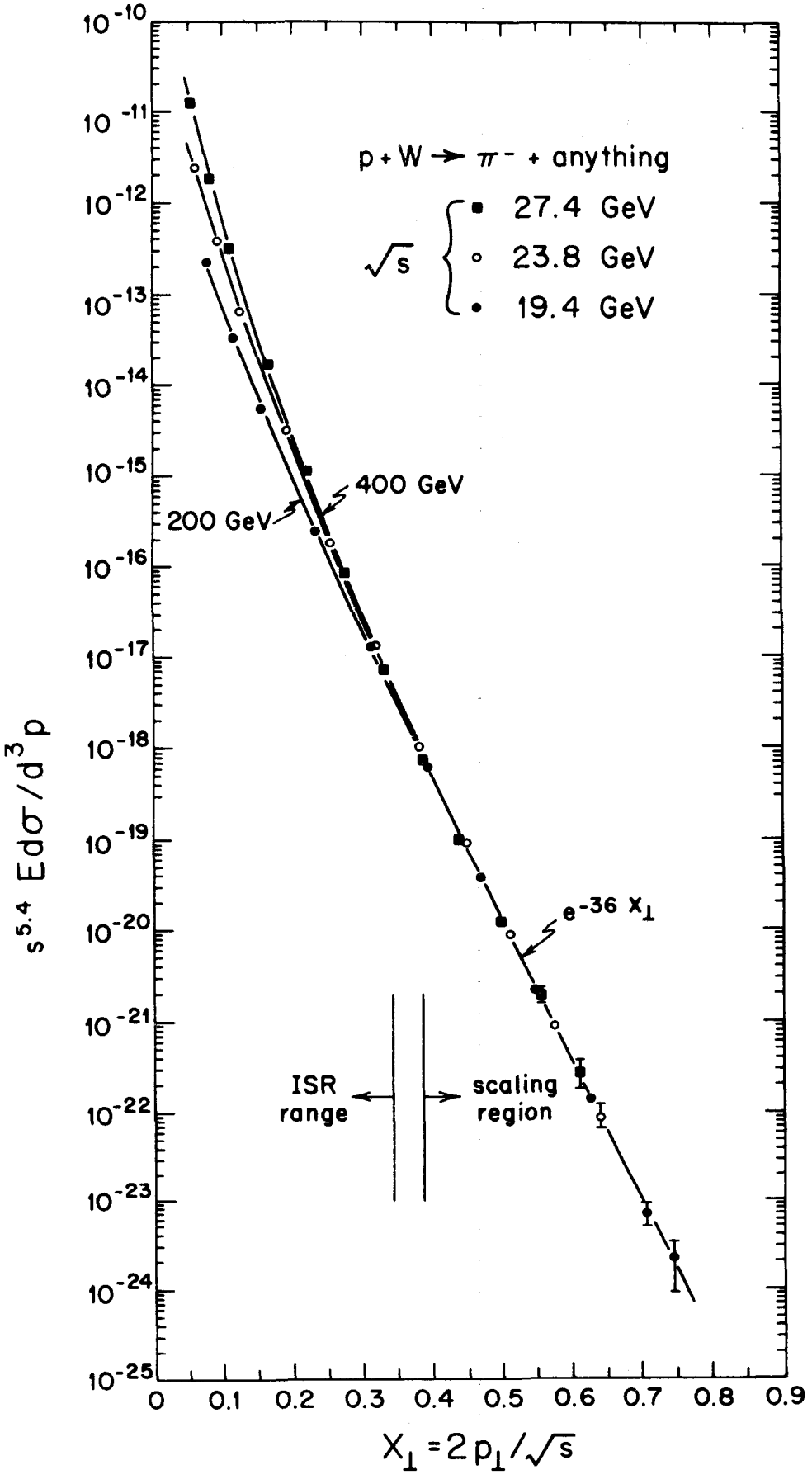
10^{-10}
10^{-11}
10^{-12}
10^{-13}
10^{-14}
10^{-15}
10^{-16}
10^{-17}
10^{-18}
10^{-19}
10^{-20}
10^{-21}
10^{-22}
10^{-23}
10^{-24}
10^{-25}
$s^{5.4}\, E d\sigma/d^3p$
$p + W \rightarrow \pi^- +$ anything
$\sqrt{s}$
27.4 GeV
23.8 GeV
19.4 GeV
200 GeV
400 GeV
$e^{-36\, X_\perp}$
ISR range
scaling region
0
0.1
0.2
0.3
0.4
0.5
0.6
0.7
0.8
0.9
$X_\perp = 2p_\perp/\sqrt{s}$

FIGURE 6

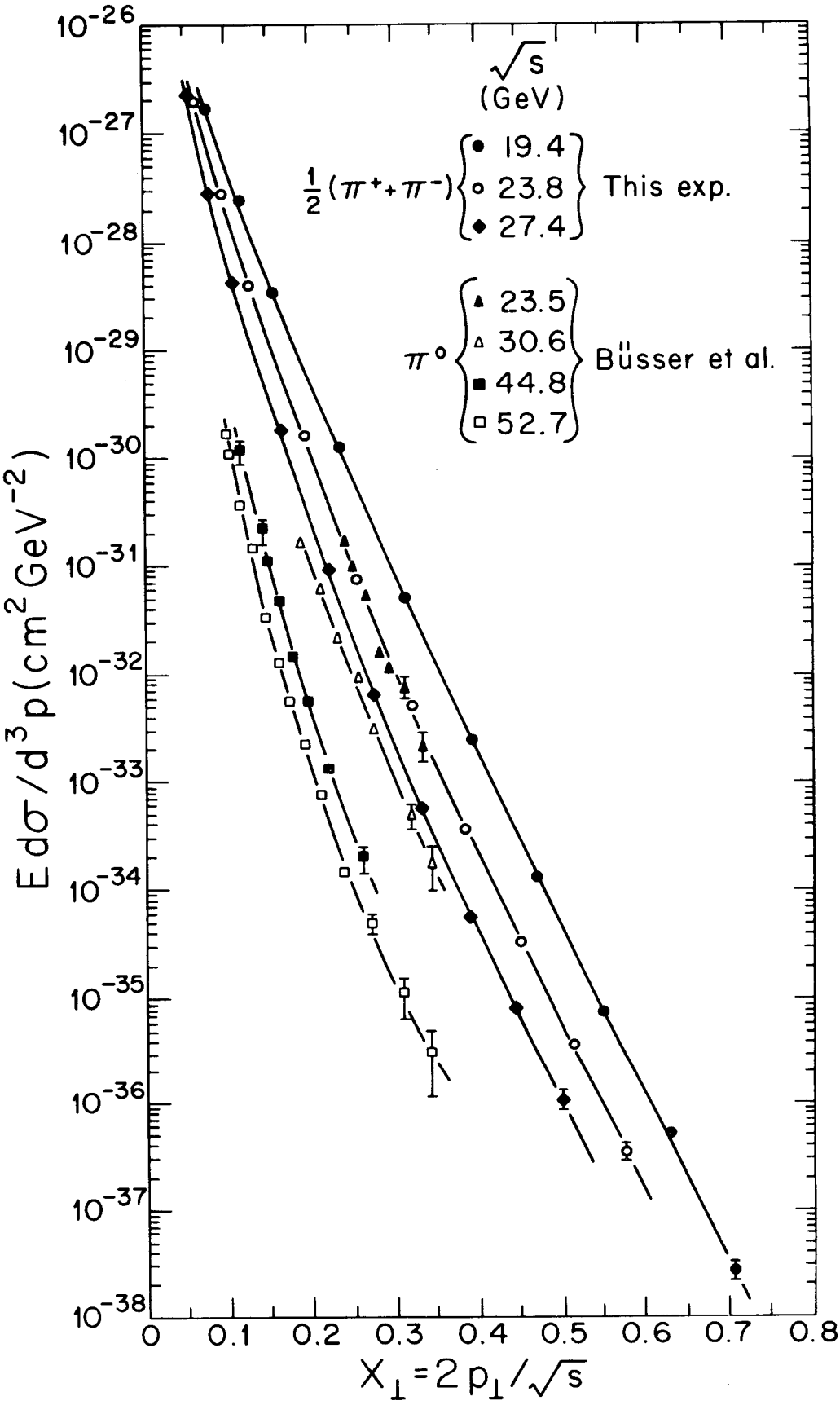
10^{-26}
10^{-27}
10^{-28}
10^{-29}
10^{-30}
10^{-31}
10^{-32}
10^{-33}
10^{-34}
10^{-35}
10^{-36}
10^{-37}
10^{-38}
$E d\sigma/d^3p (cm^2 GeV^{-2})$
0
0.1
0.2
0.3
0.4
0.5
0.6
0.7
0.8
$X_\perp = 2p_\perp/\sqrt{s}$
$\sqrt{s}$ (GeV)
$\frac{1}{2}(\pi^+ + \pi^-)$
19.4
23.8
27.4
This exp.
π^0
23.5
30.6
44.8
52.7
Büsser et al.

FIGURE 7

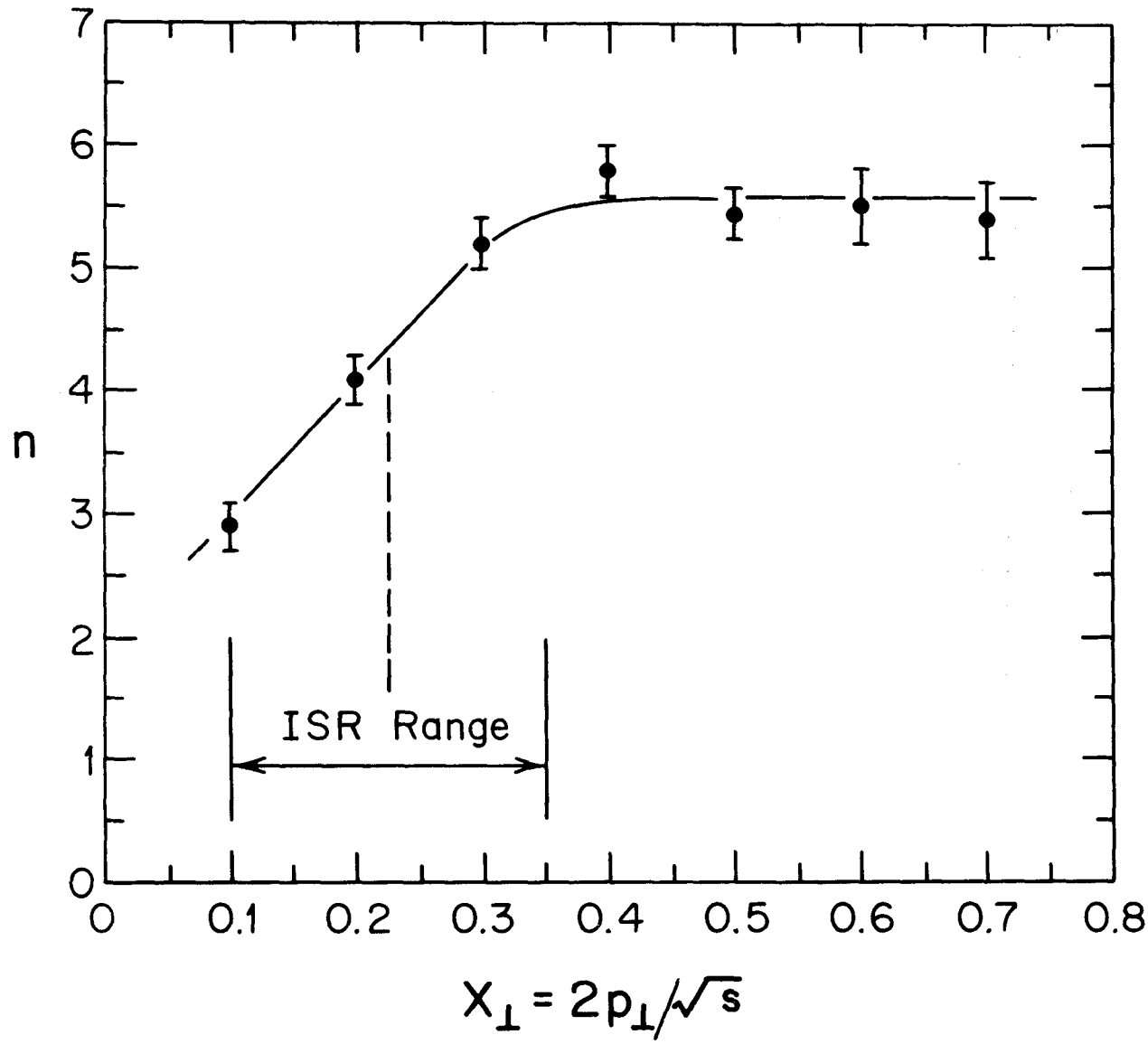
7
6
5
4
3
2
1
0
n
0
0.1
0.2
0.3
0.4
0.5
0.6
0.7
0.8
ISR Range
$X_\perp = 2p_\perp/\sqrt{s}$

FIGURE 8

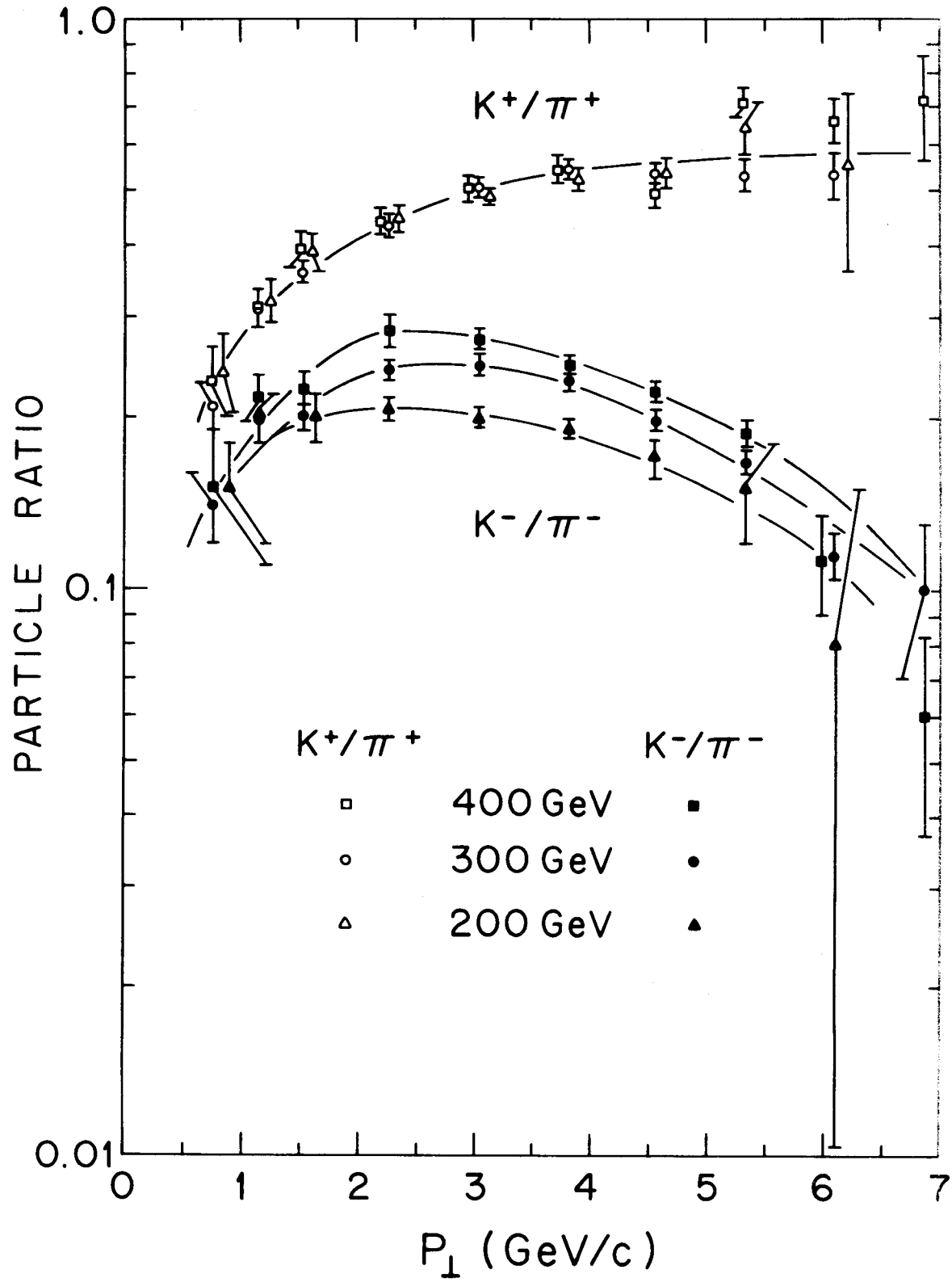
1.0
0.1
0.01
PARTICLE RATIO
K+/π+
K-/π-
K+/π+
K-/π-
400 GeV
300 GeV
200 GeV
0
1
2
3
4
5
6
7
P⊥ (GeV/c)

FIGURE 9

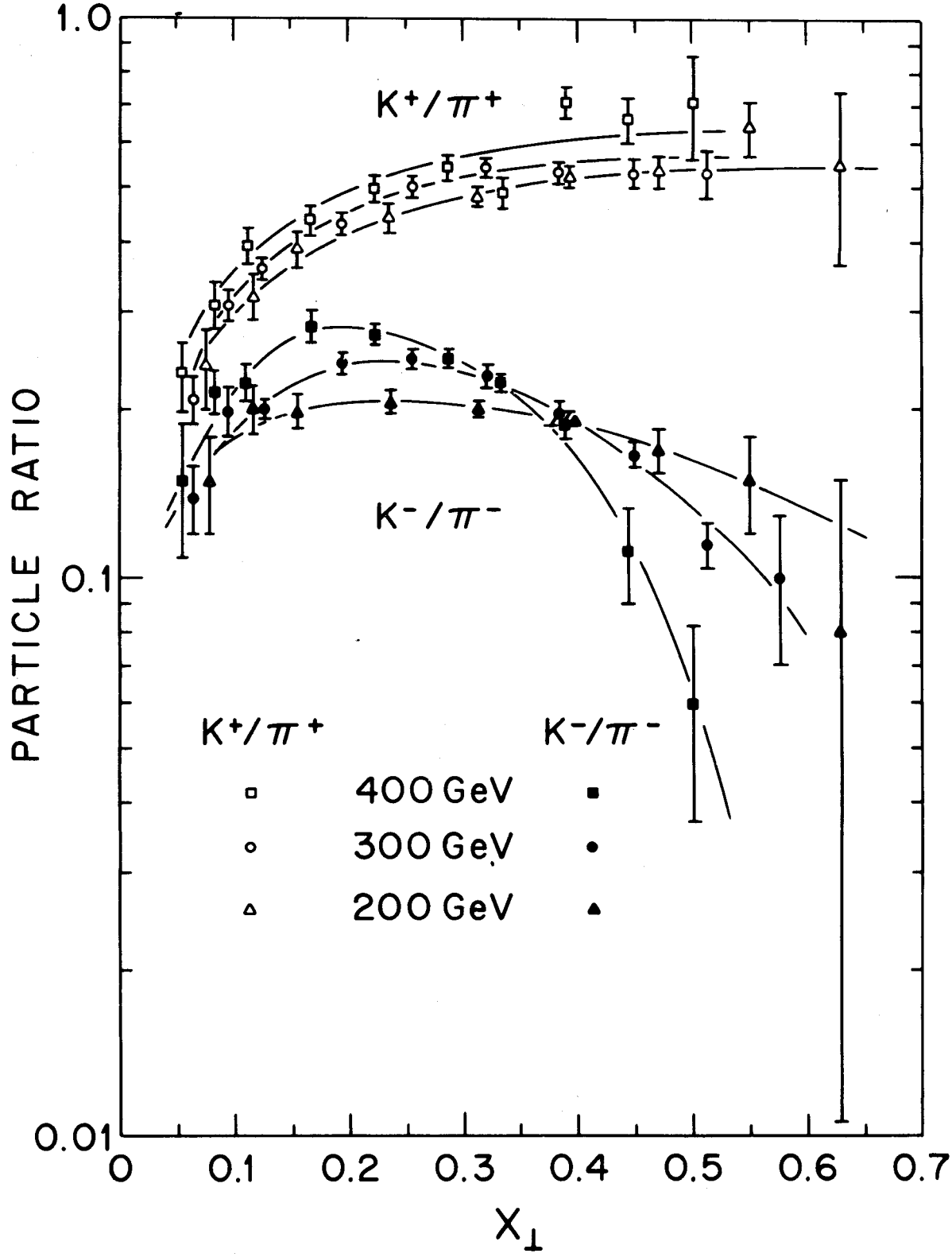
1.0
0.1
0.01
PARTICLE RATIO
K+/π+
K-/π-
K+/π+
K-/π-
400 GeV
300 GeV
200 GeV
0
0.1
0.2
0.3
0.4
0.5
0.6
0.7
X⊥

FIGURE 10

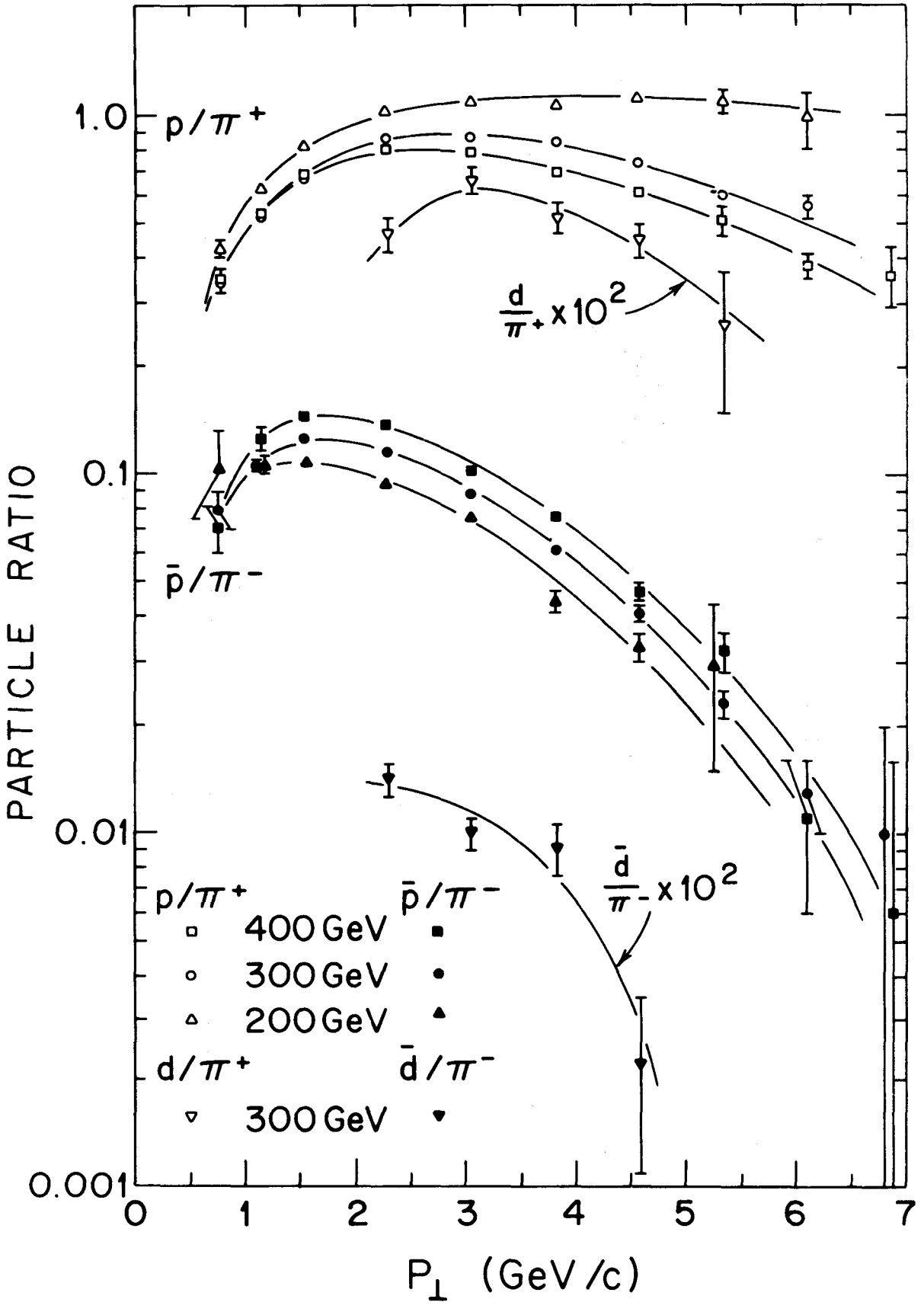
1.0
0.1
0.01
0.001
PARTICLE RATIO
p/π+
p̄/π−
d/π+ x 10²
d̄/π− x 10²
p/π+
400 GeV
300 GeV
200 GeV
d/π+
300 GeV
p̄/π−
d̄/π−
0
1
2
3
4
5
6
7
P⊥ (GeV/c)

FIGURE 11

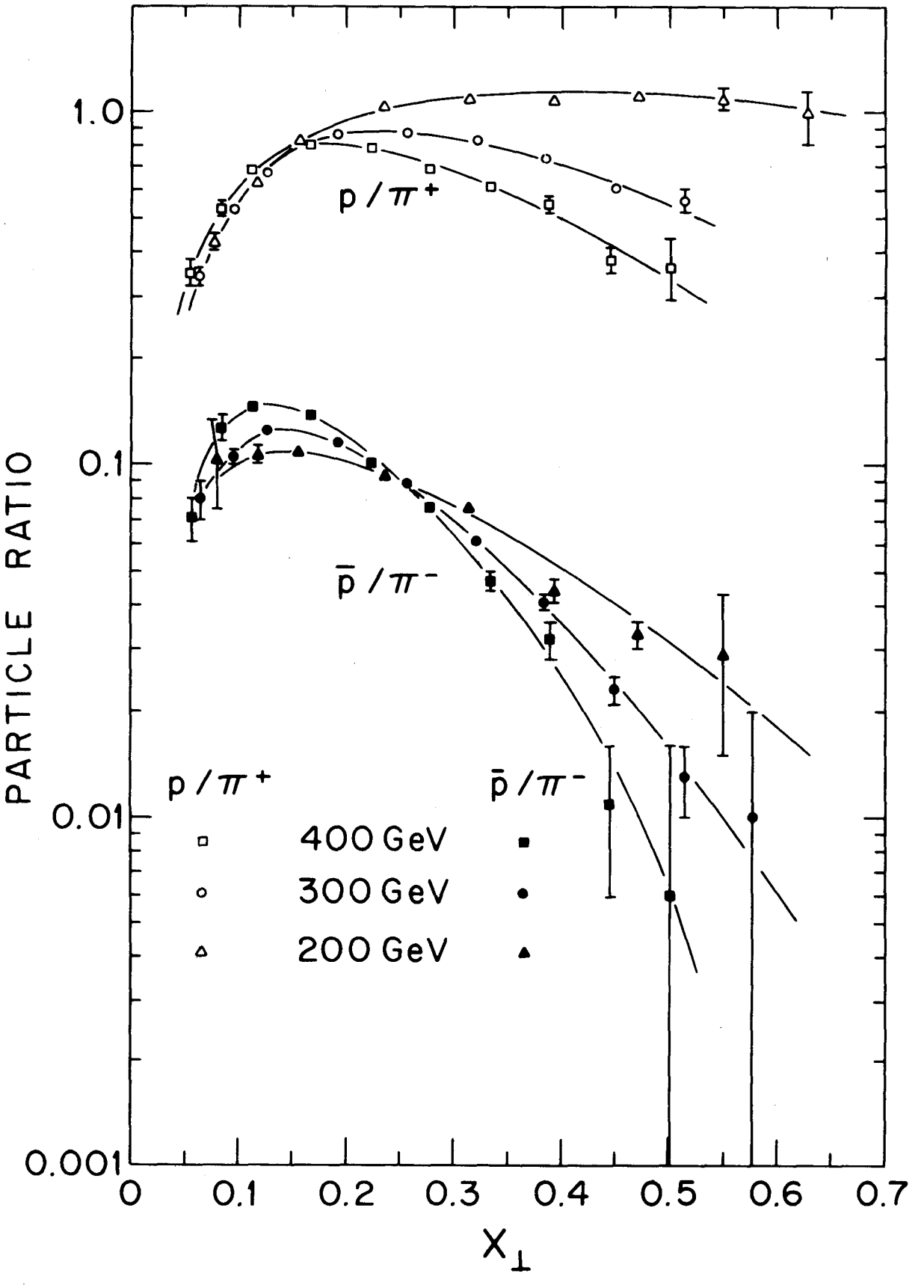
1.0
0.1
0.01
0.001
PARTICLE RATIO
p / π+
p̄ / π−
p / π+
p̄ / π−
400 GeV
300 GeV
200 GeV
0
0.1
0.2
0.3
0.4
0.5
0.6
0.7
X⊥

FIGURE 12

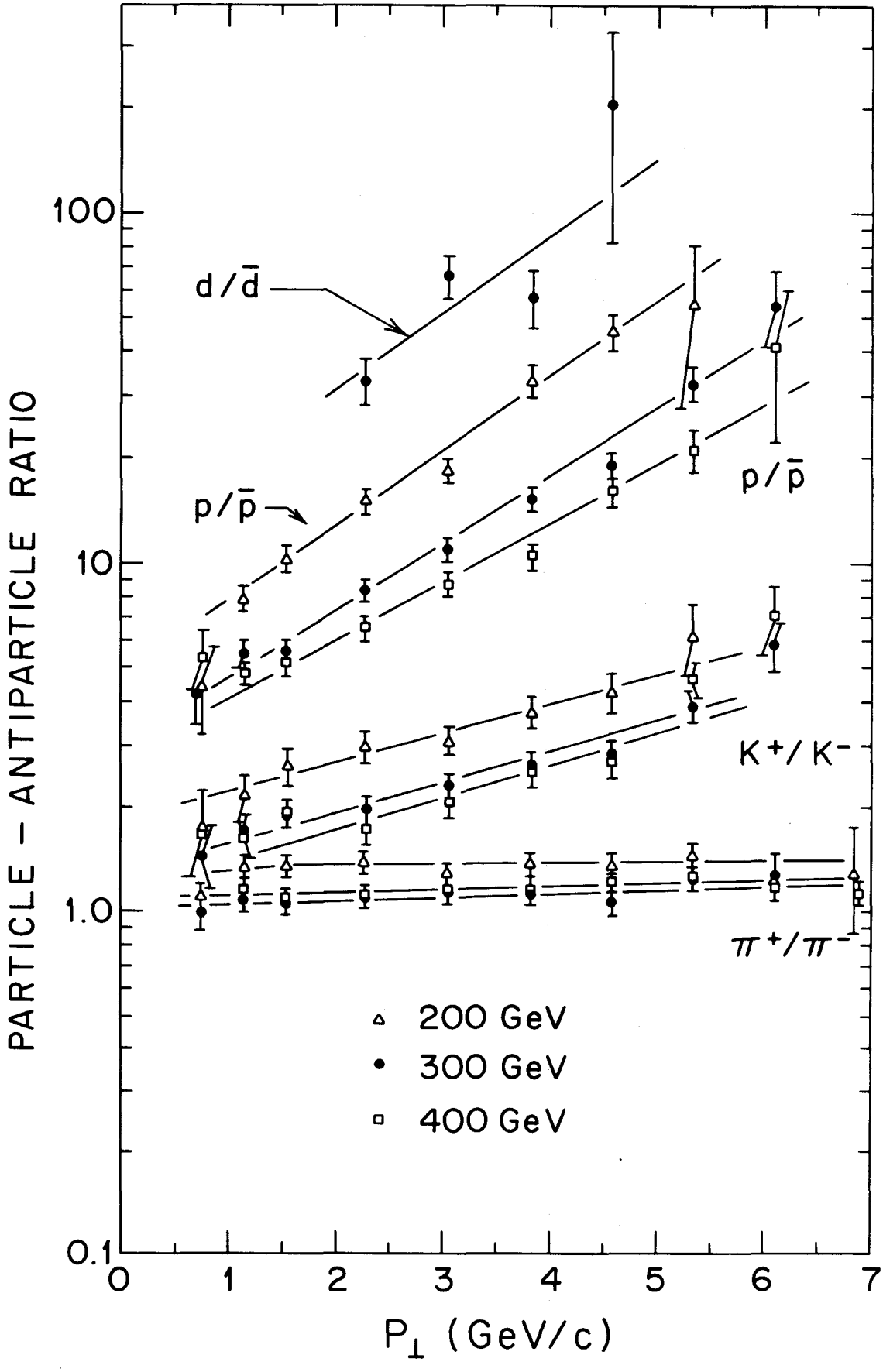
PARTICLE - ANTIPARTICLE RATIO
100
10
1.0
0.1
0
1
2
3
4
5
6
7
P⊥ (GeV/c)
d/d̄
p/p̄
p/p̄
K+/K-
π+/π-
200 GeV
300 GeV
400 GeV

FIGURE 13